Measurement of Dielectric Multipactor Thresholds at 110 GHz

S. C. Schaub, M. A. Shapiro, and R. J. Temkin

Phys. Rev. Lett. **123**, 175001 — Published 25 October 2019

DOI: 10.1103/PhysRevLett.123.175001

Measurement of Dielectric Multipactor Thresholds at 110 GHz

S. C. Schaub, M. A. Shapiro, and R. J. Temkin
Massachusetts Institute of Technology, Cambridge, MA 02139, USA
(Dated: September 4, 2019)

We report experimental measurements of the threshold for multipactor discharges on dielectric surfaces at 110 GHz. Multipactor was studied in two geometries: electric field polarized parallel to or perpendicular to the sample surface. Measured multipactor thresholds ranged from 15 to 34 MV/m, more than ten times higher than those found at conventional microwave frequencies. Measured thresholds were compared with prior data at lower frequencies, showing agreement with theoretical predictions that thresholds increase linearly with frequency. Measurements of the RF power dissipated in the multipactor show low dissipation ($\leq 1\%$) for the parallel electric field case but very strong dissipation for the perpendicular case, also in agreement with theoretical predictions. The agreement between experiment and theory over a wide range of frequencies provides a strong basis for the understanding of dielectric multipactor discharges.

Multipactor is an avalanche of free electrons on a surface exposed to radio-frequency (RF) electromagnetic fields in vacuum. It is caused by secondary emission of electrons from surfaces struck by energetic electrons that have been accelerated by the applied RF field. The phenomenon occurs in high power RF and microwave devices, often leading to the failure of vacuum windows and excessive noise in satellite communications. In RF accelerators, multipactor contributes to heat loads, beam instabilities, and detuning of resonant cavities [1].

Because of its critical importance to applications in accelerator physics [3–6], high power microwaves [7–9], and space communications [10], dielectric multipactor has become a topic of intensive research [11]. In 1998, Kishek and Lau published a model based on Monte Carlo calculations that illuminated the unique nature of multipactor on a dielectric surface, which will spontaneously charge as a multipactor develops [12]. Their model predicted the parameter space (RF and DC electric field values) where dielectric surfaces with RF electric fields parallel to the surface, e.g. RF windows, were susceptible to multipactor. Later papers expanded upon this model to explore additional physics, such as the role of the RF magnetic field or electric field angle on the parameter space of dielectric multipactor susceptibility [13–17] and new multipactor phenomena [18–20]. One of the most important predictions that has come out of these models is that the electric fields necessary to cause multipactor

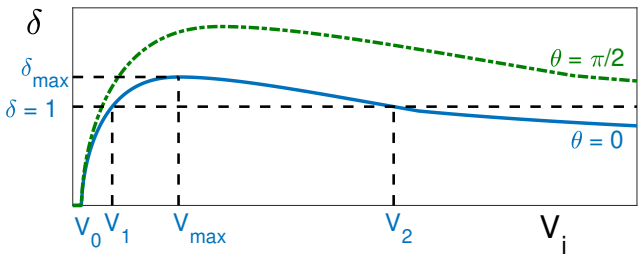

FIG. 1. Dependence of secondary electron yield, δ, on electron impact energy, V_i, and impact angle, θ [2].

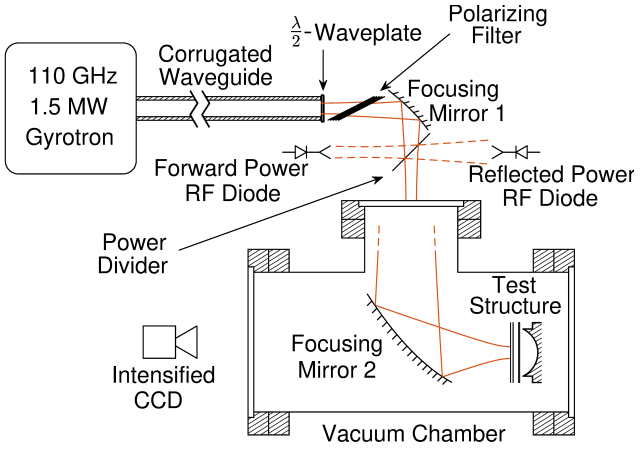

FIG. 2. Simplified schematic of the experimental setup for studying dielectric multipactor at 110 GHz. (Not to scale)

to develop (multipactor thresholds) scale linearly with frequency.

Although the calculation of multipactor thresholds is best studied with detailed theoretical analysis [12–20], the linear scaling of multipactor thresholds with frequency can be derived with a simple model. When an electron impacts a dielectric surface, the number of secondary electrons emitted from the surface (δ) can be accurately calculated from Vaughan's model of secondary electron yield (SEY) [2, 21]. This model is illustrated in Fig. 1. The curve of δ vs. impact energy, V_i, is defined by three material dependent parameters: δ_{max} is the maximum SEY for electrons impacting at normal incidence ($\theta = 0$), V_{max} is the electron impact energy at which this peak δ occurs, and V_0 is the minimum electron impact energy for nonzero SEY. V_0 is typically taken to be 12.5 eV. The lowest impact energy at which $\delta \geq 1$ is V_1, approximated by Eq. 1, derived from [2].

$$V_1 \approx \exp(-1)\delta_{max}^{-1/k_1}\,(V_{max} - V_0) + V_0 \qquad (1)$$

Here, $k_1 = 0.56$ is an empirical constant. For impacts at an oblique angle, θ, the values of δ_{max} and V_{max} both

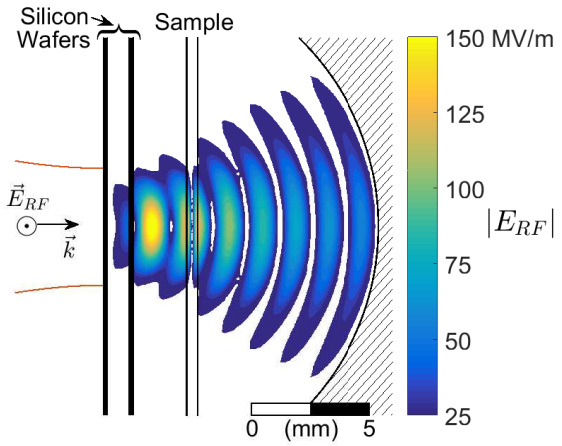

FIG. 3. Magnitude of the RF electric field excited in the $E_{\parallel}$ structure for 1 MW of input power. The peak field on the sample is 125 MV/m. Fields were calculated with ANSYS HFSS [24]

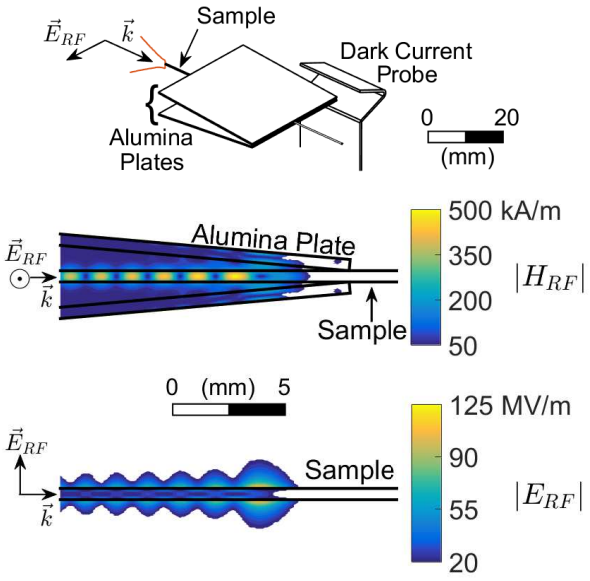

FIG. 4. Magnitude and direction of the RF magnetic and electric fields excited in the $E_{\perp}$ structure for 1 MW of power incident on a dielectric rod sample.

increase by a factor of $\left(1+\theta^2/2\pi\right)$. With RF electric fields parallel to the dielectric surface ($E_{\parallel}$), grazing impacts ($\theta \approx \pi/2$) are expected, while RF electric fields polarized perpendicular to the surface ($E_{\perp}$) lead to predominantly normal impacts ($\theta \approx 0$).

The impact energy of an electron drifting in an oscillating electric field, with negligible initial velocity is:

$$V_i = \frac{1}{2m_e}\left[\frac{eE_{RF}}{\omega}\cos\varphi\right]^2 \qquad (2)$$

In this equation, m_e and e are the electron mass and charge, respectively, ω is the angular RF frequency and φ is RF phase. To first order, when the mean impact energy of electrons is $\geq V_1$, stray electrons impacting an uncharged dielectric (no DC field) will on average yield more than one secondary electron. Multipactor will develop through subsequent impacts of secondary electrons [22]. Averaging over φ yields an electric field for the multipactor threshold, E_{MT}, which is linearly dependent on ω.

$$E_{MT} = (2\omega/e)\sqrt{m_e V_1} \qquad (3)$$

This prediction can be refined using Vaughan's model and Eq. 2 to calculate SEY as a function of phase. The theoretical E_{MT} is found as the value of E_{RF} that solves:

$$\langle\delta\rangle = \frac{1}{2\pi}\int_0^{2\pi}\delta(\varphi, E_{RF})d\varphi = 1\ . \qquad (4)$$

The value of E_{RF} which solves Eq. 4 is 10 - 20% greater than the solution to Eq. 3 for the materials studied [23]. Because, for a specified material and impact angle, Vaughan's model depends only on impact energy, Eq. 2, the linear scaling of E_{MT} with ω is preserved.

Multipactor on dielectrics was studied using a 1.5 MW gyrotron operating at 110 GHz with 3 μs pulses [25, 26]. The output of the gyrotron was coupled into the HE_{11} mode of a 31.75 mm diameter corrugated waveguide. This HE_{11} mode couples 98% to a Gaussian beam at the waveguide output [27], facilitating the manipulation of the microwave beam with optical techniques. A schematic of the experimental setup is shown in Fig. 2. At the waveguide output, a half-waveplate was used with a polarizing filter (quartz slabs at a Brewster angle) to serve as a continuously variable attenuator. Inside the vacuum chamber, maintained below 10^{-8} Torr, one of two test structures was mounted, to study multipactor with either $E_{\parallel}$ or $E_{\perp}$ RF surface fields on the test samples. Materials studied are listed in Table I.

Calibrated RF diodes monitored power into and reflected from the test structures. Power reflected from the structures was small and had a negligible effect on gyrotron operation. An intensified CCD (ICCD) detected visible light emission from multipactor. An electrically floating dark current probe mounted on each test structure detected energetic electrons that drifted out of a multipactor discharge.

The $E_{\parallel}$ test structure, shown at the beam waist in Fig. 2, is shown in greater detail in Fig. 3. This was a Gaussian beam-mode cavity, designed to study multipactor in a geometry similar to that of an RF window. The 110 GHz beam was focused to a 2.5 mm (0.92λ) radial spot

Material	δ_{max}	V_{max} [eV]	Expt. $E_{MT\parallel}$ [MV/m]	Eq. 4 $(E_\parallel)$ [MV/m]	Expt. $E_{MT\perp}$ [MV/m]	Eq. 4 $(E_\perp)$ [MV/m]
Alumina	6	400	15	13	28	14
Sapphire (ground)	6.4	650	N/A	15	29	16
Sapphire (polished)	7.8	650	26	14	N/A	14
Fused Quartz	2.9	420	30	20	34	22
Crystal Quartz	3.8	400	25	17	N/A	18

TABLE I. Experimental multipactor thresholds, E_{MT}, as a function of RF geometry. The tested samples had a polished surface in the $E_\parallel$ structure, and a ground surface in the $E_\perp$ structure, with the exception of fused quartz, which was always polished. Material parameter values are from [33–37]. The values shown for alumina, a ceramic, are typical for high purity material, but the SEY varies between vendors. Alumina was sourced from Insaco Inc. and CoorsTek for $E_\parallel$ and $E_\perp$ testing, respectively. Theoretical values from Eq. 4 assume a mean impact angle of $\theta = \pi/2$ for the $E_\parallel$ geometry and $\theta = 0$ for the $E_\perp$ geometry.

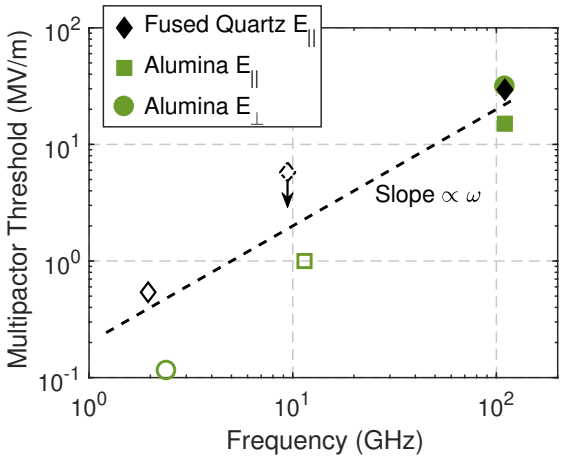

FIG. 5. Dielectric multipactor thresholds at frequencies from 2 to 11 GHz [3, 22, 37, 38] are compared with the present data at 110 GHz (filled symbols). Data include $E_\parallel$ geometry for fused quartz (diamonds) and alumina (squares) as well as $E_\perp$ geometry for alumina (circles). The dashed line is drawn to illustrate the theoretical linear dependence of threshold field on frequency and is not a fit to the data.

size on a 96.7% reflective semitransparent mirror consisting of two silicon wafers separated by 900 μm. The cavity formed between the semitransparent mirror and a reflecting spherical copper mirror contained the sample under test at the second field maximum along the axis of symmetry (see Fig. 3). The spherical mirror was mounted on a piezoelectric actuator, allowing tuning of the cavity resonance.

The $E_\perp$ test structure is illustrated in Fig. 4. The incident 110 GHz beam was focused to a 1.5 mm (0.55λ) radial spot size on the end of a thin dielectric rod. This rod served as both a waveguide and the sample under test. The microwave beam excited an HE_{11} mode of a solid dielectric rod [28–32] with about 90% coupling of the incident power. The dielectric rod supported only one confined mode. The diameter of each rod was chosen to maximize the surface electric field of the excited mode (0.5 mm for alumina and sapphire, 0.8 mm for fused quartz). Sapphire rods had c-axis orientation. To provide field enhancement, two alumina plates were placed at a 5 degree angle above and below the dielectric rod. The sides of these plates that formed the top and bottom of the structure, away from the sample, were metalized. This cut off the dielectric rod mode at the end of the taper formed by the two plates, setting up a standing wave along the rod.

Multipactor thresholds were measured by slowly increasing the incident microwave power until multipactor was detected on the three diagnostics (ICCD, dark current, reflected power). Within experimental uncertainty, all diagnostics measured the same thresholds for each material and geometry. Results are collected in Table I. The reproducibility of the measured thresholds from sample to sample was better than $\pm$ 1 MV/m. The total uncertainty in the measured thresholds was dominated by the precision of the RF power measurement and was estimated as $\pm$ 2 MV/m. Comparison in Table I of measured thresholds with numerical solutions to Eq. 4 shows the model to underpredict the experimental values. This may be partly due to the assumption of homogeneous RF fields in the model.

Fig. 5 shows a plot of E_{MT} vs. frequency for fused quartz and alumina. The measured thresholds at 110 GHz are compared to measurements by other groups at 2 - 11 GHz [3, 22, 37, 38]. Though multipactor damaging of RF windows has long been a topic of research, the bulk of published studies have focused on the maximum power a window can tolerate before suffering damage [39, 40], rather than documenting RF intensities at which multipactor first develops. As a result, there are few quantitative measurements of multipactor thresholds to which we can compare our data at 110 GHz. The plotted data point for fused quartz at 9.4 GHz is an upper limit, due to the indirect multipactor detection method used in that study[38]. The data in Fig. 5 are consistent with the theoretical prediction of an approximately linear increase in E_{MT} with increasing frequency. This is an important result for the application of high power microwave sources at sub-THz and THz frequencies. The resultant high values of the multipactor threshold at high frequencies are very helpful in avoiding the onset of multipactor.

Theoretical studies predict very different physical parameters of a steady state dielectric multipactor dis-

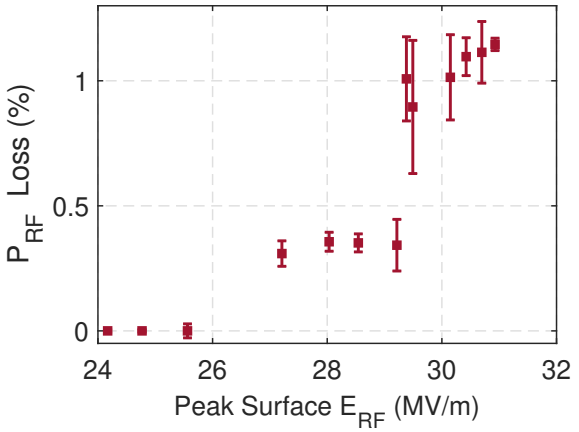

FIG. 6. Measured power dissipated ($P^{\|}_{loss}/P_{in}$) due to multipactor on a sapphire sample in the $E_{\|}$ structure.

charge depending upon RF field geometry. With $E_{\|}$, the dielectric is predicted to charge until electrons impact with a mean energy of V_1, a few 10's of eV, with electron trajectories short compared to an RF period. Power deposited on a dielectric by electron impacts can be calculated as:

$$P_{loss} = N \langle V_i \rangle / \tau \tag{5}$$

where N is the number of electrons, $\langle V_i \rangle$ is the mean impact energy, and τ is the mean time between impacts. It was derived in [41] that this leads to a simple result for the RF loss in a single pass through an RF window, Eq. 6. For $E_{\|}$, $P^{\|}_{loss}$ is given by:

$$P^{\|}_{loss}/P_{in} \approx 4 \times 10^{-3} \sqrt{V_{0m}/(1 \text{ eV})} \ , \tag{6}$$

where V_{0m} is the most probable initial kinetic energy of secondary electrons, taken to be $0.005 \times V_{max}$. The derivation of Eq. 6 assumes homogeneous RF fields. Monte Carlo calculations of a fully developed dielectric multipactor[12, 41], indicate that electrons have short time of flight between impacts, << than an RF period, leading to trajectories that are very small compared to the RF wavelength. In a steady state dielectric multipactor, electrons essentially sample a homogeneous RF field.

In experiment, power dissipated by multipactor was monitored using the calibrated reflected power RF diode shown in Fig. 2. The results with $E_{\|}$ are presented in Fig. 6. The power loss due to multipactor in one cavity round trip (two passes through the sample) suddenly jumps to 0.4% near 26 MV/m as one side of the sample develops multipactor. The fractional power dissipation then stays constant within experimental uncertainty until a second jump occurs as the second side of the sample (at slightly lower field) develops a multipactor discharge. The peak field to which the $E_{\|}$ structure could be tested was limited by the multipactor discharge shifting the resonant frequency of the cavity structure at very high incident powers. The observed power dissipation is lower than the prediction of Eq. 6, using a V_{max} of 650 eV, by about a factor of four (Eq. 6 is for a single pass through a single-sided multipactor). However, the predicted low value ($\leq$1%) of loss and the independence of loss vs. E_{RF} are clearly observed.

With $E_{\perp}$, the dielectric surface is predicted to charge until electrons have resonant trajectories, taking an integer number of RF cycles (most probably 1) from launch to return to the dielectric surface ($\tau \approx 2\pi/\omega$). These resonant electrons gain an average energy of

$$\langle V_i \rangle = \frac{2}{m_e} \left(\frac{\pi e E_{DC}}{\omega} \right)^2 \ , \tag{7}$$

amounting to 100's to 1000's of eV as derived in [3]. E_{DC} is the DC electric field that arises from charging of the dielectric. From Monte Carlo studies, at E_{RF} above E_{MT}, the value of E_{DC} to which the dielectric surface charges is approximately linearly proportional to E_{RF}, as can clearly be seen in multipactor susceptibility plots such as those in [3, 5, 23]. Defining $E_{DC} = \alpha E_{RF}$, α is found to range from 0.3 to 0.33 for the materials tested. The number of electrons in the multipactor can be estimated using Gauss's law as $N = \varepsilon_0 A E_{DC}/e$, where A is the effective area of the multipactor discharge, about 4.5 mm^2 in our $E_{\perp}$ test structure. Calculating loss at E_{RF} above E_{MT}, using Eq. 5, leads to:

$$\frac{P^{\perp}_{loss}}{P_{in}} = \frac{\pi e \varepsilon_0}{m_e \omega} \frac{\alpha^3}{\beta} A \left(E_{RF} - E_{MT} \right) \ . \tag{8}$$

The constant β is the proportionality between input RF power and surface RF fields: $P_{in} = \beta E^2_{RF}$. For the experiment shown in Fig. 4, $\beta = 6.4 \times 10^{-11}$ Wm^2/V^2 for the $E_{\perp}$ structure. Fig. 7 shows power dissipation measured in the $E_{\perp}$ test structure. Very good agreement is obtained between the measured values and the theoretical values from Eq. 8 for $P^{\perp}_{loss}/P_{in}$ above the threshold field E_{MT} (≈29 MV/m). The observed linear relationship between fractional power loss and E_{RF} contrasts clearly with the independence of loss vs. E_{RF} seen in the $E_{\|}$ structure.

The present study has measured dielectric multipactor thresholds for various materials as a function of RF field geometry. The linear scaling of multipactor thresholds with frequency is experimentally supported, a promising result for future applications at sub-THz and THz frequencies. This conclusion is based on the available results and would be strengthened by further testing of the materials listed in Table I at other frequencies. Measurements also verify the predicted stark difference in the power dissipated by dielectric multipactor between $E_{\|}$ and $E_{\perp}$ geometries. In agreement with published theory, power loss through a dielectric in the $E_{\|}$ (window) geometry is small and independent of RF intensity. Power

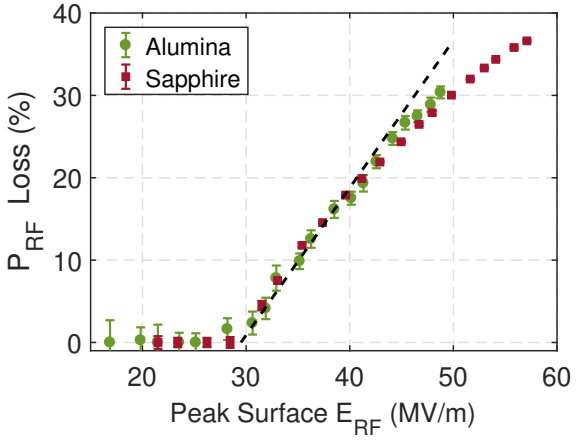

FIG. 7. Measured power dissipated ($P^{\perp}_{loss}/P_{in}$) due to multipactor with $E_{\perp}$ on samples of sapphire and alumina. The dashed line is Eq. 8, using values of α, β and A described in the text. Eq. 8 is evaluated using the peak surface value of E_{RF}.

loss with a strong $E_{\perp}$ component, such as in a dielectric loaded waveguide, grows linearly with the RF field, and can lead to high losses within a small surface area. The excellent agreement between experiment and theory demonstrates a very good physical understanding of dielectric multipactor.

This research was supported the Department of Energy, Office of High Energy Physics under Grant No. DE-SC0015566 and the Office of Fusion Energy Sciences through Grant No. DE-FC02-93ER54186.

[1] A. W. Chao, K. H. Mess, M. Tigner, and F. Zimmermann, *Handbook of Accelerator Physics and Engineering*, 2nd ed. (World Scientific, 2013).
[2] R. Vaughan, IEEE Trans. Electron Devices **40**, 830 (1993).
[3] J. G. Power, W. Gai, S. H. Gold, A. K. Kinkead, R. Konecny, C. Jing, W. Liu, and Z. Yusof, Phys. Rev. Lett. **92**, 164801 (2004).
[4] C. Jing, C. Chang, S. H. Gold, R. Konecny, S. Antipov, P. Schoessow, A. Kanareykin, and W. Gai, Appl. Phys. Lett. **103**, 213503 (2013).
[5] L. Wu and L. K. Ang, Phys. Plasmas **14**, 013105 (2007).
[6] O. V. Sinitsyn, G. S. Nusinovich, and T. M. Antonsen, Phys. Plasmas **16**, 073102 (2009).
[7] R. J. Barker and E. Schamiloglu, *High-Power Microwave Sources and Technologies* (IEEE Press, New York, 2001).
[8] A. Neuber, D. Hemmert, H. Krompholz, L. Hatfield, and M. Kristiansen, J. Appl. Phys. **86**, 1724 (1999).
[9] C. Chang, G. Liu, C. Tang, C. Chen, and J. Fang, Phys. Plasmas **18**, 055702 (2011).
[10] T. P. Graves, *Standard/Handbook for Multipactor Breakdown Prevention in Spacecraft Components* (Aerospace Corp. Report No. TOR-2014-02198, El Segundo, CA, USA, 2014).
[11] R. A. Kishek, Y. Y. Lau, L. K. Ang, A. Valfells, and R. M. Gilgenbach, Phys. of Plasmas **5**, 2120 (1998).
[12] R. A. Kishek and Y. Y. Lau, Phys. Rev. Lett. **80**, 193 (1998).
[13] A. Sazontov, V. Semenov, M. Buyanova, N. Vdovicheva, D. Anderson, M. Lisak, J. Puech, and L. Lapierre, Phys. Plasmas **12**, 093501 (2005).
[14] A. G. Sazontov and V. E. Nechaev, Phys. Plasmas **17**, 033509 (2010).
[15] A. G. Sazontov, V. E. Nechaev, and N. K. Vdovicheva, Appl. Phys. Lett. **98**, 161503 (2011).
[16] A. G. Sazontov, V. E. Nechaev, and N. K. Vdovicheva, IEEE Trans. Plasma Sci. **40**, 451 (2012).
[17] A. S. Sakharov, V. A. Ivanov, and M. E. Konyzhev, Plasma Phys. Reports **39**, 1122 (2013).
[18] R. A. Kishek, Phys. Rev. Lett. **108**, 035003 (2012).
[19] E. Sorolla, M. Belhaj, J. Sombrin, and J. Puech, Phys. Plasmas **24**, 103508 (2017).
[20] H. Wang, D. Liu, L. Liu, M. Xie, and L. Meng, Plasma Sources Sci. Technol. **27**, 125006 (2018).
[21] J. R. M. Vaughan, IEEE Trans. Electron Devices **36**, 1963 (1989).
[22] A. S. Sakharov, V. A. Ivanov, Y. A. Tarbeeva, and M. E. Konyzhev, Plasma Phys. Reports **38**, 1090 (2012).
[23] S. C. Schaub, *Studies of Dielectric Multipactor Discharges and Gas Breakdown Initiated by High Power Millimeter Waves*, Ph.D. thesis, Massachusetts Institute of Technology, Cambridge, MA USA (2019).
[24] Ansys, Inc., Ansys electronics desktop [online]. available: www.ansys.com 2015.
[25] D. S. Tax, E. M. Choi, I. Mastovsky, J. M. Neilson, M. A. Shapiro, J. R. Sirigiri, R. J. Temkin, and A. C. Torrezan, J. Infrared Millim. Terahertz Waves **32**, 358 (2011).
[26] J. M. Neilson, R. L. Ives, S. C. Schaub, W. C. Guss, G. Rosenzweig, R. J. Temkin, and P. Borchard, IEEE Trans. Electron Devices **65**, 2316 (2018).
[27] M. A. Shapiro and R. J. Temkin, J. Infrared Millim. Terahertz Waves **32**, 283 (2011).
[28] C. Yeh and F. I. Shimabukuro, The essence of dielectric waveguides (Springer, New York, 2008) pp. 137–150.
[29] E. Snitzer, J. Opt. Soc. Am. **51**, 491 (1961).
[30] P. J. B. Clarricoats, Proc. IEEE Part C: Monographs **108**, 170 (1961).
[31] D. Marcuse, Bell Syst. Tech. J **49**, 1695 (1970).
[32] A. W. Snyder, IEEE Trans. Microw. Theory Tech **17**, 1138 (1969).
[33] O. Hachenberg and W. Brauer, Secondary electron emission from solids (Academic Press, New York, 1959) pp. 413–499.
[34] P. H. Dawson, J. Appl. Phys. **37**, 3644 (1966).
[35] Suharyanto, Y. Yamano, S. Kobayashi, S. Michizono, and Y. Saito, IEEE Trans. Dielectr. Electr. Insul. **13**, 72 (2006).
[36] B. Song, W. Shen, H. Mu, J. Deng, X. Hao, and G. Zhang, IEEE Trans. Plasma Sci. **41**, 2117 (2013).
[37] R. B. Anderson, W. D. Getty, M. L. Brake, Y. Y. Lau, R. M. Gilgenbach, and A. Valfells, Rev. Sci. Instr. **72**, 3095 (2001).
[38] O. A. Ivanov, M. A. Lobaev, V. A. Isaev, and A. L. Vikharev, Phys. Rev. ST Accel. Beams **13**, 022004 (2010).
[39] Y. Saito, IEEE Trans. Dielectr. Electr. Insul. **2**, 243 (1995).
[40] A. Miura and H. Matsumoto, in *Proc. Int. Conf. Part.*

Accel. (1993) pp. 1124–1126 vol.2.

[41] L. K. Ang, Y. Y. Lau, R. A. Kishek, and R. M. Gilgenbach, IEEE Trans. Plasma Sci. **26**, 290 (1998).